SAND2018-11935J

3-D modeling of induced seismicity along multiple faults: magnitude, rate and location in a poroelasticity system

K. W. Chang[1], H. Yoon[2]

[1]Geotechnology & Engineering Department, Sandia National Laboratories, Albuquerque, New Mexico, USA.

[2]Geoemchanics Department, Sandia National Laboratories, Albuquerque, New Mexico, USA.

Key Points:

- Multiple faulting system is modeled in a three-dimensional (3-D) domain including poroelastic coupling.
- Pore-pressure diffusion and/or poroelastic stressing induce seismicity along the fault with any hydraulic type.
- The 3-D modeling captures properly the hydraulic and mechanical interaction between faults and surrounding formations.

Corresponding author: K. W. Chang, kchang@sandia.gov

Sandia National Laboratories is a multimission laboratory managed and operated by National Technology & Engineering Solutions of Sandia, LLC, a wholly owned subsidiary of Honeywell International Inc., for the U.S. Department of Energy's National Nuclear Security Administration under contract DE-NA0003525.

Abstract

Understanding of the potential to injection-induced seismicity along faults requires the response of fault zone system to spatio-temporal perturbations in pore pressure and stress. In this study, three-dimensional (3-D) model system consisting of the caprock, reservoir, and basement is intersected by vertical strike-slip faults. We examine the full poroelastic behavior of the formation and perform the mechanical analysis along each fault zone using the Coulomb stress change. The magnitude, rate and location of potential earthquakes are predicted using the spatial distribution of stresses and pore pressure over time. Rapid diffusion of pore pressure into conductive faults initiates failure, but the majority of induced seismicity occurs at deep fault zones due to poroelastic stabilization near the injection interval. Less permeable faults can be destabilized by either delayed pore-pressure diffusion or poroelastic stressing. A two-dimensional (2-D) horizontal model, representing the interface between the reservoir and the basement, limits diffusion of pore pressure and deformation of the formation in the vertical direction that may over- or underestimate the potential of earthquakes along the fault. Our numerical results suggest that the 3-D modeling of faulting system including poroelastic coupling can reduce the uncertainty in the seismic hazard prediction by considering the hydraulic and mechanical interaction between faults and bounding formations.

1 Introduction

The recent increase of induced seismicity has been linked to subsurface energy activities involving injection operations such as wastewater injection related to conventional oil and gas development [*Ellsworth*, 2013; *Kerenan et al.*, 2013; *Hough*, 2014; *Rubinstein et al.*, 2014], geothermal energy production [*Giardini*, 2009], or geological CO_2 sequestration [*White and Foxall*, 2016]. The majority of large seismic events ($M_W > 3$) was observed within the basement rocks (or lowermost sediments) below the injection interval where large faults are involved [*Horton*, 2012; *Kim*, 2013; *Verdon*, 2014; *Hornbach et al.*, 2015]. The mechanical failure of the fault depends on the orientation and location of the fault, the in-situ state of stress, and the hydrogeological and mechanical properties of the intermediate sequences between the fault and injection interval [*Segall*, 1989; *Zhang et al.*, 2013; *Figueiredo et al.*, 2015; *Chang et al.*, 2018]. Two major mechanisms have been suggested to explain the occurrence of injection-induced seismicity associated

with fault instability : (1) direct diffusion of pore pressure and (2) indirect transfer of poroelastic stresses [*Ellsworth*, 2013; *Chang and Segall*, 2016a].

Injection-induced increase of pore pressure will perturb the state of stress near/on the pre-existing faults, and may initiate fault slips [*Hubbert and Rubbey*, 1959]. The impact of direct diffusion of increased pore pressure on the fault stability is influenced by both hydraulic and elastic properties of the formation (e.g., permeability and elastic moduli) which will control the extent of the pressure propagation [*Zhang et al.*, 2013; *Chang and Segall*, 2016a]. The areal extent of the pressurized region over time commonly attributes to the reactivation of pre-existing faults, potentially the spatial distribution induced seismicity [*Seeber et al.*, 2004; *Ake et al.*, 2005; *Arrowsmith and Eisner*, 2006].

Indirect stress transfer can also cause rock deformation, subsequently destabilizing the pre-existing fault without substantial changes in pore pressure fields [*Ellsworth*, 2013; *Chang and Segall*, 2016a]. The interaction between fluid flow and solid elastic deformation perturbs stress fields inside and even outside the pressurized region, which can be described by poroelastic coupling, not by the diffusion-driven process only. The poroelastic coupling has an impact on the fields of pore pressure and stresses were observed in the well operation sites [*Segall*, 1989; *Hills*, 2000; *Gambolati et al.*, 2010], which are not negligible for modeling a fluid-saturated rock [*Detournay and Cheng*, 1993; *Zimmermann*, 2000].

To solve for the strong interaction between the fluid and solid phases, numerical coupling schemes are required to integrate fluid flow and solid deformation in space and time. Two typical coupling schemes, either iteratively or fully coupled, are employed. For an iterative coupling approach, either the mechanical or flow problem is solved first, followed by the other problem using an intermediate solution until the solution converges within an acceptable tolerance [*Settari and Mourits*, 1998; *Settari and Walters*, 2001; *Tran et al.*, 2004; *Jha and Juanes*, 2007; *Wheeler and Gai*, 2007; *Kim et al.*, 2011]. For a fully coupled approach as in this study, the mechanical response and flow variables are calculated simultaneously through a system of equations for geomechanics and flow at every time step [*Pan et al.*, 2009; *White and Borja*, 2011]. Compared to the iterative coupling scheme, the fully coupled approach is unconditionally stable, but requires the development of a unified flow-geomechanics simulator with proper constitutive models, which is computationally more expensive.

To predict the induced seismicity caused by fluid injection and develop mitigation strategies of induced seismic events, it is important to improve our understanding of the physical mechanisms between injection activities and the (re)activation of faults. In particular, there is a strong need to study the pressure propagation/retardation from the injector in different fault zone systems (e.g., conductive vs. sealing) and poroelastic relationships between pressure distribution and critically stressed faults. Operational conditions of fluid injection such as the total volume of fluid injected [*McGarr*, 2014] and the injection rate [*Weingarten et al.*, 2015; *Langenbruch and Zoback*, 2016; *Chang et al.*, 2018] can influence the degree of induced seismicity (e.g., number of events and magnitude). More importantly, fault-zone properties such as hydrogeological and geomechanical properties, host rock lithology, and fault zone architecture are key to predicting the poroelastic response of fault system under in-situ pressure and stress conditions [*Caine et al.*, 1996; *Rinaldi et al.*, 2014; *Figueiredo et al.*, 2015]. The fault can also transform a laterally extensive formation into compartments. Each compartment surrounding the fault has its own hydrogeological and mechanical characteristics and the presence of discontinuity along each compartment will control on the migration of fluids within and through each compartment. For example, the low permeable fault hinders fluid flow across the fault that causes the variability in the pressure field on either side of the fault, possible resulting in shear failure along the fault plane [*Chang and Segall*, 2016a; *Vilarrasa et al.*, 2016].

Recent geomechanical modeling of injection-induced seismicity along the fault implemented a 2-D vertical domain including a single fault with a plane strain condition [*Rutqvist et al.*, 2016; *Zbinden et al.*, 2017; *De Simone et al.*, 2017]. Full 3-D modeling of reactivation of a single fault was performed to simulate the potential seismicity associated with shale-gas fracturing [*Rutqvist et al.*, 2015] and geological CO_2 storage [*Rinaldi et al.*, 2015]. At a regional scale, however, multiple fault sets are generally observed and their spatial distribution may generate a heterogeneous stress field [*Maerten et al.*, 2002; *Duan and Oglesby*, 2006]. Some 2-D studies modeled the multiple faulting system in the basement rock, but identical properties often applied to each fault [*Chang and Segall*, 2016a,b], in which the distance from the well is the only factor determining the stability of each fault at given formation properties. Hydraulic properties of each fault influence the dynamics of fluid flow, giving rise to the spatio-temporal pressure field corresponding to the injection operations. Also, joints and small-scale faults may elevate or

reduce the fault permeability that causes localized pressurization along the fault. As a result, induced seismicity was commonly observed at intersections or bends in basement faults [*Doser et al.*, 1992] due to variable seismic response to changes in pore pressure.

Since the fault zone architecture is complex and very difficult to be accurately accounted for, the fault systems have been simply treated as single features with hydraulic and mechanical properties without considering heterogeneity and anisotropy of hydromechanical properties inside the fault zone [e.g., *Bense and Person*, 2006; *Gudmundsson et al.*, 2010; *Rinaldi et al.*, 2014]. If the thickness of the fault zone is negligible compared to the overall reservoir scale, the mechanical behavior of the thin fault zone can be represented by zero-thickness mechanical interfaces [e.g., *Day and Potts*, 1994; *Parson*, 2002; *Cappa and Rutqvist*, 2011; *Jha and Juanes*, 2014]. However, a large contrast of mechanical properties (e.g., bulk and shear moduli) along the fault can cause numerical instability [*Day and Potts*, 1994], so careful selection of the interface properties is required. Hydraulic elements can be added along the interface to account for the effect of pore pressure perturbations on the fault stability [*Cappa and Rutqvist*, 2011]. The comparative study of implementing finite-thickness elements or mechanical interfaces with equivalent mechanical properties shows that hydromechanical behavior of faults driven by fluid flow can be represented properly with either method [*Cappa and Rutqvist*, 2011]. Our numerical scheme using finite-thickness elements easily implements a variety of fault characteristics (from a homogeneous fault plane to a complex fault zone), which is more appropriate for simulating the fault instability caused by fluid injection.

The objective of this study is to enhance our mechanistic understanding of induced seismicity in the presence of multiple faults by evaluating spatio-temporal distributions of stresses and pore pressure, consequently the magnitude and rate of potential earthquakes. We model a 3-D domain with a three-layer system (units of mudrock, reservoir, and basement) including multiple faults that intersect the reservoir and basement. The mechanical response of the formation to the well operation (injection/shut-in) is quantified by the changes in pore pressure and stresses. For the comparative analysis, 2-D simulation of the interface between the reservoir and basement is performed to evaluate if 2-D models will address the same mechanistic behaviors compared to 3-D simulations. This comparative study validates the effect of diffusion and deformation in an extra dimension on the perturbation in pore pressure and stresses, potentially the earthquake occurrence along the fault plane.

2 Model Description

2.1 Governing equations

To model the injection-induced coupling process, we adapt the linear poroelasticity theory [e.g., *Biot*, 1941] that describes mechanical equilibrium and fluid mass conservation in terms of the displacement field $\mathbf{u}$ and pore pressure p as follows [*Biot*, 1941; *Rice and Cleary*, 1976; *Wang*, 2000; *Segall*, 2010]:

$$\nabla \cdot [G(\mathbf{x}) \nabla \mathbf{u}] + \nabla \left[\frac{G(\mathbf{x})}{1 - 2\nu(\mathbf{x})} \right] \nabla \cdot \mathbf{u} - \alpha(\mathbf{x}) \nabla p + \mathbf{f} = 0, \tag{1}$$

$$S(\mathbf{x}) \frac{\partial p}{\partial t} - \frac{1}{\eta} \nabla \cdot [k(\mathbf{x}) \nabla p] = -\alpha(\mathbf{x}) \frac{\partial}{\partial t} (\nabla \cdot \mathbf{u}) \tag{2}$$

where the shear modulus (G, Pa) and the Poisson's ratio (ν, -) are for drained conditions and $\mathbf{f}$ is the body force per unit volume of the bulk. The Biot-Willis coefficient α (-) represents the ratio of changes in the fluid volume to the total bulk volume for deformation at constant pore pressure, defined as

$$\alpha = \frac{3(\nu_u - \nu)}{B(1 - 2\nu)(1 + \nu_u)} \tag{3}$$

where the Poisson's ratio ν_u and Skempton's coefficient (B, -) are for undrained conditions ($\Delta m = 0$). B is the ratio of the change in pore pressure to the change in mean normal stress. Note that only two of three parameters (ν_u, B, and α) are independent. In the conservation equation (2), k (m^2) is the permeability, η (Pa·s) is the fluid viscosity, and S (Pa^{-1}) is the constrained specific storage [*Wang*, 2000]. S represents the increase of the amount of fluid (per unit volume of rock) as a result of a unit increase of pore pressure, under constant volumetric strain ($\epsilon = 0$) given by

$$S = \frac{\alpha^2 (1 - 2\nu)(1 - 2\nu_u)}{2G(\nu_u - \nu)}. \tag{4}$$

Full poroelastic coupling is represented by the presence of ∇p in equation (1), acting as body forces in the stress equilibrium, and $\nabla \cdot \mathbf{u}$ in the flow equation (2).

2.2 Model domain

Assuming that faults are well-oriented for slip in the given stress state, small perturbations in stresses or pore pressure can induce the instability of the faults [*Stein*, 1999]. As shown in Figure 1a, the 3-D numerical domain has three layers of mudrock, reservoir, and basement with 200 m, 25 m, and 1 km of thickness, respectively. The laterally ex-

tensive geometry (5 km×5 km) is employed to minimize the boundary effects due to pore-pressure diffusion caused by water injection. The domain includes three vertical strike-slip faults with strike of N30W. Each fault, 5 m wide and 1 km long, extends up to the top of the reservoir and down to the bottom of the basement (1.025 km high, but not intersecting the mudrock layer). The fault width is selected as a median value from the thickness-displacement relationship based on the field and microstructural data of the fault zone [*Wibberley et al.*, 2008]. The faults are modeled as two end-member types for a typical range of the permeability: high-permeability (conductive) faults (Faults 1 and 3, $k_{f1} = k_{f3} = 1 \times 10^{-12}$ m^2) and a low-permeability (sealing) fault (Fault 2, $k_{f2} = 1 \times 10^{-21}$ m^2). For the sensitivity test of the fault permeability effect, the permeability of sealing Fault 2 is increased by six orders of magnitude (sealing into moderately conductive, $k_{f2} = 1 \times 10^{-15}$ m^2), while the other Faults 1 and 3 remain the same. Hydrogeological and mechanical properties of the reservoir and faults are given in Table 1. The 3-D domain is reduced by the cross-sectional surface throughout the center of the faults where the symmetric conditions are satisfied, to enhance numerical efficiency.

A single-phase fluid is uniformly injected into the center of the 3-D domain at a constant mass rate of 0.02 kg/m/s during the injection period (Δt =30 days). A total simulation time is 60 days to investigate post shut-in behavior. Since we are concerned with perturbations from the equilibrium state, the initial stresses and pore pressure are set to zero in this work. A top boundary has a constant pore-pressure condition ($p = 0$) and is free to move in all directions, while a bottom boundary has no-flow condition ($\nabla p = 0$) and is free to move in the surface-parallel direction only. Side boundaries have a constant pore-pressure condition and are free to move in the surface-parallel direction.

The governing equations (1) and (2) are numerically solved with initial and boundary conditions to study the perturbation in pore pressure and stresses driven by fluid injection as well as after shut-in. The finite-element analysis is performed using COMSOL Multiphysics 5.3 [*COMSOL Multiphysics*, 2017]. A variable step method is employed for time integration [*Dreij et al.*, 2011], and tetrahedral/mapped elements are used for spatial discretization [*Hughes*, 2000]. Mesh is highly refined near faults and the injection point to resolve the strong gradients of pore pressure and displacement (Figure 1b).

2.3 Coulomb failure analysis

To characterize the failure of the pre-existing fault caused by fluid injection, the modified Coulomb failure criterion has been widely used, $\tau_s = f(\sigma_n + p)$ where τ_s and σ_n are the shear and normal stresses acting on the fault surface, respectively. The coefficient of fault friction (f) is assumed constant as a standard laboratory value [*Zoback and Healy*, 1992]. For the critically stressed faults, the mechanical stability of the faults is effectively quantified by the change in Coulomb stress, $\Delta\tau \equiv \Delta\tau_s + f(\Delta\sigma_n + \Delta p)$ using a extension positive convention. To evaluate the poroelastic effects, we rearrange $\Delta\tau$ in terms of the changes in poroelastic stresses and pore pressure [*Chang and Segall*, 2016a; *Chang et al.*, 2018]:

$$\Delta\tau(\mathbf{x}, t) = [\Delta\tau_s(\mathbf{x}, t) + f\Delta\sigma_n(\mathbf{x}, t)] + f\Delta p(\mathbf{x}, t) \tag{5}$$

where $\Delta\tau_s$ is the change in shear stress, $\Delta\sigma_n$ is the change in normal stress, and Δp is the change in pore pressure. In equation (5), positive values of $\Delta\tau$, $\Delta\tau_s$, and $\Delta\sigma_n$ imply that the fault plane is moved closer to failure, the change in shear stress favors failure in the expected slip direction of the fault (here taken to be strike-slip), and an increase in relative tension across the fault, respectively.

2.4 Seismicity magnitude estimate in poroelastic medium

The magnitude of a seismic event (M_{W}) is a measure of earthquake size to predict the ground motion as well as potential damage. For the seismic hazard associated with fluid injection, M_{W} can be determined by the injection parameters (i.e., rate and period) and/or the hydrogeological and mechanical properties of the geological formation.

The maximum magnitude of induced seismicity may be limited by the total volume of fluid injected into the fully saturated formation (ΔV) which is related to the maximum seismic moment ($M_{0,max}$) as [*McGarr*, 2014]

$$M_{0,max} = \frac{(1.5 - b)}{b} 2fK\Delta V \tag{6}$$

where b is defined in the classic Gutenberg-Richter (G-R) frequency-magnitude relation (higher b-value implies more small earthquakes relative to larger events) and K (Pa) is the bulk modulus for drained conditions ($\Delta p = 0$) measuring the volumetric strain due to changes in applied stress while holding pore pressure constant.

Consideration of poroelastic deformation driven by fluid injection yields the following formula to predict the maximum magnitude of injection-induced earthquakes (refer to Appendix A for details):

$$M_{0,max} = \frac{(1.5-b)}{b}\frac{2f}{S}\Delta V \tag{7}$$

where the inverse of the constrained specific storage (S^{-1}, Pa; refer to the equation (4)) is the Biot's modulus. It is noted that these two approaches based on ΔV do not account for the local characteristics of the fault zone (e.g., fault geometry and strength) and the variability of lithology and formation properties, neglecting the localized gradients of pore pressure and stresses.

The spatio-temporal variation of the b-value depends on geological factors (e.g., formation heterogeneity [*Mogi*, 1962], anomalous stress distribution [*Wyss*, 1973], or thermal gradients [*Warren and Latham*, 1970]). The evolution of pore pressure driven by fluid injection can be linked to the spatio-temporal variation of the b-value [*Bachmann et al.*, 2012]. At the geothermal stimulation site at Basel, Switzerland, the b-value varies in the range from 1.1 to 1.6 corresponding to the location relative to the injection point and the phase of injection operations (higher b-value closer to the injector during the injection period). The b-value of induced earthquakes is generally higher than normal tectonic events [*Shapiro et al.*, 2011], and this study assumes $b = 1.38$ (mean b-value from Table 1 in *Dempsey et al.* [2016]) for the prediction of earthquake magnitudes.

By correlating the fault geometry to mechanical deformation, the seismic magnitude can be correlated to the total amount of displacement on the fault during the seismic event. The seismic moment on an individual fault plane can be measured by the following formula [*Kanamori and Brodsky*, 2001]:

$$M_0 = G\bar{\mathbf{u}}A \tag{8}$$

where $\bar{\mathbf{u}}$ (m) is the average displacement along the fault surface and A (m^2) is the rupture area. The formula can be expressed in terms of the integral of displacement over the fault plane area

$$M_0 = G\int \mathbf{u}dA. \tag{9}$$

Assuming that faults are located nearby the injection well close enough to be pressurized by direct diffusion, the rupture area is identical to the size of the whole fault zone and independent of the propagation of the pressure front. This approach, thus, excludes local dynamics of the fault instability driven by time-dependent processes (i.e., pore-pressure

diffusion into the fault zone and subsequent deformation) and may constrain the upper limit of the magnitude for induced earthquakes on individual fault.

The G-R frequency-magnitude distribution of earthquakes can be expressed in terms of seismic moment M_0 (N-m), which defines the moment-magnitude relation as follows [*Hanks and Kanamori*, 1979]

$$M_{\mathrm{W}} = \frac{2}{3}\left[\log_{10} M_0 - 9.05\right]. \tag{10}$$

2.5 Seismicity rate prediction

The rate of earthquakes at given magnitudes can be estimated by the seismicity rate model developed by [*Dieterich*, 1994] as in the previous studies [*Chang and Segall*, 2016a,b]. Assuming that the ratio of shear stress to effective normal stress, $\tau_s/\bar{\sigma} = \tau_s/(\sigma_n + p)$ is constant, we obtain the following formulation as follows:

$$\frac{dR}{dt} = \frac{R}{t_a}\left(\frac{\dot{\tau}}{\dot{\tau}_0} - R\right) \tag{11}$$

where R (-) is the seismicity rate relative to an assumed steady-state seismicity rate at a background stressing rate ($\dot{\tau}_0$) and $t_a \equiv a\bar{\sigma}/\dot{\tau}_0$ is the characteristic relaxation time for seismicity to restore to steady state.

In this study, we assume that the fault constitutive friction parameter ($a = 0.003$) quantifies the direct effect in the rate-state friction law, and the background effective stress ($\bar{\sigma} = 13.33$ MPa) acts on the fault plane. The background stressing rate ($\dot{\tau}_0$) is assumed to be 10^{-3} MPa/yr such that a typical 1 MPa stress drop accumulates in 10^3 years. This leads to a characteristic time of $t_a = 40$ years.

Equation (11) relates the Coulomb stress changes to the seismicity rate changes. The numerical simulation generates spatiotemporal distributions of Coulomb stress (5) on the point (or surface) we concern, and the stressing rate ($\dot{\tau}$) is calculated by curve-fitting functions. Then, we solve the ordinary differential equation (11) to obtain $R(\mathbf{x}, t)$ on the fault using the Matlab ODE solver `ode45`. The details of the numerical procedure can be found in [*Chang and Segall*, 2016a; *Chang et al.*, 2018].

3 Numerical Results

3.1 Pressure and stress distributions in the 3-D model

Figure 2 shows the distribution of $f\Delta p$, $\Delta\tau_s + f\Delta\sigma_n$, and $\Delta\tau$ in the 3-D space at the end of injection ($t = 30$ days). We use the same color scheme for all simulation results (red for positive value and blue for negative), and the green contour line represents the value of 0.02 MPa.

The conductive fault near the injector (Fault 1) enhances strong pore-pressure buildup due to rapid direct diffusion whereas the sealing fault (Fault 2) inhibits the pore-pressure propagation across it (Figure 2a). Small increase in pore pressure is observed at the conductive fault far away from the injector (Fault 3) due to late diffusion around the sealing fault at the given injection period and rate.

Pressure buildup causes strong compression (negative $\Delta\tau_s + f\Delta\sigma_n$) within the reservoir and shallow basement whereas relatively weak extension (positive $\Delta\tau_s + f\Delta\sigma_n$) below the pressurized regions (Figure 2b). Both dilation of the pressurized regions and confinement of pore pressure causes strong compression outside the sealing Fault 2 at shallow depth. Physical mechanisms of poroelastic stressing will be discussed in the section 4.1.

The distribution of the Coulomb stress change ($\Delta\tau$) is similar to the $f\Delta p$ distribution in a lateral direction, implying that pore-pressure diffusion significantly contributes to the instability of the diffusion-dominant regions (Figure 2c). Poroelastic stressing results in positive $\Delta\tau$ at deep basement and outside the sealing fault where pore pressure does not diffuse directly.

Figure 3 shows the temporal data of $f\Delta p$, $\Delta\tau_s + f\Delta\sigma_n$, and $\Delta\tau$ along the middle of each fault. The vertical axis of each plot is from the fault top (boundary between the mudrock and the reservoir at $x_3 = 0.025$ km) while the lower bound is at $x_3 =$ -0.4 km. The dash line at $t = 30$ days in each plot represents the end of injection.

Direct pore-pressure diffusion leads to positive $f\Delta p$ throughout the conductive Fault 1 nearest the injection well (Figure 3a). Pore fluid continues to spread out, and the maximum $f\Delta p$ is achieved after shut-in. Low permeability of Fault 2 inhibits direct pore-pressure diffusion into/across it, but still poroelastic stressing perturbs the pressure field (Figure 3b). Most of meaningful changes in $f\Delta p$ are observed at the upper portion of

Fault 2 because the permeability contrast between the fault and surrounding reservoir generates intense mechanical response to lateral diffusion. Fault 2, acting as a hydraulic barrier, prevents substantial pore-pressure diffusion into the conductive Fault 3 far away from the injector, but slow and steady increases in $f\Delta p$ is observed along Fault 3 even after shut-in (Figure 3c).

The poroelastic coupling effect can be determined by either compression within or extension outside the pressurized regions where diffusion is dominant. Poroelastic compression (negative $\Delta\tau_s + f\Delta\sigma_n$) develops within the entire conducive Fault 1 where pore pressure diffuses (Figure 3d). The sealing Fault 2 within the injection interval ($0 \leq z \leq 0.025$ km) is compressed due to its resistance against the expansion of bounding reservoir (Figure 3e). Below the injection interval ($z \leq 0$ km) is initially extended with poroelastic expansion of the surrounding basement. Later (including the post shut-in phase) pore pressure diffuses in the basement rock that compresses the shallow portion of the fault. The distant conductive Fault 3 is slightly compressed by delayed pore-pressure diffusion (Figure 3f).

Positive $\Delta\tau$ develops along the entire Fault 1, but poroelastic compression reduces the direct impact of elevated pore pressure on the upper portion of Fault 1 (Figure 3g). Poroelastic extension of the basement rock causes positive $\Delta\tau$ along the Fault 2, even without direct diffusion of pore pressure (Figure 3h). Fault 3 is initially stabilized by poroelastic compression, and later destabilized due to post shut-in diffusion of pore pressure (Figure 3i).

3.2 Estimate of the maximum earthquake magnitude

For the injection scenario (the net injected fluid volume $\Delta V \approx 1.3\times10^3$ m^3) and fault properties as listed in Table 1, the seismic moment and magnitude of potential earthquakes induced by fluid injection are calculated (Table 2). The maximum seismic moment is predicted to be 1.08×10^{12} N·m using the McGarr's method (equation 6), equivalent to a moment magnitude of 1.99 from the moment-magnitude relation (10). Note that a larger injection rate for a longer period will increase ΔV, which will increase the upper limit of M_{W} based on the linear relation between $M_{0,max}$ and ΔV (equation 6).

With poroelastic deformation caused by fluid injection (equation 7), the maximum seismic moment is estimated to be 1.66×10^{12} N·m, equivalent to the maximum magni-

tude of 2.11. The reservoir tends to dilate with increasing the fluid volume by injection, while the elastic surrounding formations resist and compress the reservoir. This poroelastic compression within the pressurized reservoir is compensated by larger Δp, corresponding to larger ΔV from the linear relation (A.4). This would enhance the upper bound to the earthquake magnitude, resulting in a larger magnitude than that from the equation (6).

The spatial distribution of displacement along the surface of an individual fault is obtained along the middle of the vertical fault plane at every time step. The seismic moment along each fault and the maximum magnitude are computed using the equations (9) and (10), respectively. The largest magnitude ($M_{\mathrm{W},max} = 1.47$) is generated on the conductive Fault 1 mainly due to direct diffusion of pore pressure into the Fault 1. Even without pore-pressure diffusion into the sealing Fault 2, poroelastic expansion of basement rocks surrounding the Fault 2 results in substantial displacement ($M_{\mathrm{W},max} = 1.35$). The predicted $M_{\mathrm{W},max}$ along each fault plane is less than those estimated by ΔV because the $\bar{u}$-based estimate excludes dissipation of pore pressure and subsequent mitigation of stresses into upper/lower formations surrounding faults. Although the earthquake magnitude estimated in this study was relatively low, the estimate of $M_{\mathrm{W},max}$ could increase dramatically depending on the injection operation (e.g., larger injection rate and longer periods) and/or the formation characteristics (e.g., hydrogeological and mechanical properties, fault geometry favorable to the fault instability and/or the presence of fractures/faults directly connecting to the injection interval).

3.3 Estimate of the seismicity rate along each fault

Using temporal data of $\Delta\tau$, the seismicity rate model (equation 11) gives the evolution of the seismicity rate (R) along the middle of each fault (Figure 3j to 3l). The seismicity rate (R) increases on any type of faults, but the controlling mechanism varies depending on the fault permeability and location.

Substantial increment in R is predicted along the deep Fault 1 ($z < -0.25$ km) due to the combined effect of direct pore-pressure diffusion and corresponding poroelastic compression (Figure 3j). The maximum R ($R_{max} \approx 24$) is observed after the end of injection because the post shut-in relaxation of poroelastic compression is much faster than the pressure front retarded under an undrained condition [*Chang and Segall*, 2016a].

Depending on the fault permeability, the synergy between delayed diffusion of pore pressure and poroelastic stressing can cause dramatic increases in R after shut-in [*Chang et al.*, 2018]. A modest rise in R is estimated along the sealing Fault 2 below the reservoir ($R_{max} \approx 4$, -0.05 km $< z < 0$ km) driven mainly by poroelastic extension (Figure 3k). Along the distant Fault 3, post shut-in diffusion causes small and slow increases in R ($R_{max} \approx 1.4$) at the deep fault zone (Figure 3l). Note that the injection operation with higher rates and/or longer periods will cause more diffusion into the conductive fault, and potentially enhance the rate of earthquakes along the fault.

4 Discussion

4.1 Effect of poroelastic coupling

Figure 4 schematically describes physical mechanisms of poroelastic deformation driven by fluid injection. Diffusion of pore pressure into conductive structures (reservoir and conductive faults) enlarges the pressurized region (blue), whereas the extent of the pressure plume in a vertical direction is relatively limited by low permeable bounding units (mudrock and basement). The pore-pressure diffusion in the conductive pathways generates the extension at the adjacent basement, which subsequently compresses the basement at the distance. Inside the pressurized region strong compression develops due to poroelastic response of the rock solid to pore-pressure buildup. On the other hand, a sealing fault acts as flow barriers, leading to abrupt changes in the pore pressure field across the fault. Without direct pore-pressure diffusion into the sealing fault (where $\Delta\tau \approx \Delta\tau_s + f\Delta\sigma_n$), poroelastic stressing perturbs the stress state inside the sealing fault by two primary mechanisms: (1) compression of the upper fault surrounded by the pressurized reservoir and shallow basement, enhancing the fault stability and (2) extension at the deep fault outside the pressurized region, potentially generating earthquakes (refer to the subplot of Figure 4). Note that the location and rate of injection-induced earthquakes will vary depending on injection scenarios and fault zone characteristics (e.g., geometry, location, hydrogeological and mechanical properties).

To highlight the impact of poroelastic coupling on the induced seismicity, the uncoupled problem, where the mechanical deformation is neglected and the fluid flow is solved independently of the stress field, is simulated. For quantitative comparison, all simulation conditions are maintained to be the same for both coupled and uncoupled simula-

tions. The conditions of uniaxial strain ($\epsilon_{11} = \epsilon_{22} = 0$) and constant vertical stress ($\sigma_{33} = c$) reduces the flow equation (2) to the standard transient flow equation as follows:

$$S_u(\mathbf{x})\frac{\partial p}{\partial t} - \frac{1}{\eta}\nabla \cdot [k(\mathbf{x})\nabla p] = 0 \tag{12}$$

where S_u (Pa^{-1}) is the uniaxial specific storage expressed as

$$S_u = S + \frac{\alpha^2 (1-2\nu)}{2G(1-\nu)}. \tag{13}$$

The uncoupled system perturbs pore-pressure fields only, indicating that $\Delta\tau = f\Delta p$ and $\Delta\tau_s = f\Delta\sigma_n = 0$. As a result, pore pressure in the conductive Fault 1 increases dramatically, but does not change in the sealing Fault 2 (Figures 5a to 5b). Pore pressure increases slightly in the conductive Fault 3 due to a delayed diffusion through the sealing Fault 2 (Figure 5c), but the degrees of the change is minimal.

In the uncoupled system, the seismicity rate (R) is a function of the pore-pressure change only ($R \sim f\dot{p}$) due to the absence of poroelastic stressing. Hence, R is estimated to be high along the Fault 1 ($R_{max} \approx 150$), whereas R to be close to the background rate ($R \sim 1$) in both Faults 2 and 3 (Figures 5d to 5f). The R values propagate from the upper to lower parts of the model domain corresponding to the pore-pressure propagation, and the maximum R is observed at the uppermost fault zone within the reservoir.

When the geomechanical response to fluid injection is neglected, direct diffusion of pore pressure into the conductive fault through hydraulic pathways is the only mechanism to induce seismicity as discussed in previous studies [e.g., *Zhang et al.*, 2013; *Kerenan et al.*, 2014; *Nakai et al.*, 2017; *Hearn et al.*, 2018]. Thus, the observed seismicity along deep basement faults can be accounted for only by the extent of the pressure plume through the undetected pathways (e.g., permeable fault or fracture networks) hydraulically connecting between the pressurized region and the deep part of the conductive fault.

Our coupled model, however, shows that injection-induced perturbations in pore pressure and/or stresses can induce seismicity in various hydraulic types of basement fault. For conductive faults, direct diffusion causes significant changes in pore pressure throughout the fault. However, poroelastic compression suppresses seismicity at the shallow fault zone, such that most of earthquakes will occur at the deep fault zone. This mechanism may explain the observation that the majority of injection-induced earthquakes occurred

within the basement, 1 to 4 km deeper than the reservoir [*Seeber et al.*, 2004; *Horton*, 2012; *Kim*, 2013]. For sealing faults, limited diffusion results in negligible pore-pressure change within them, but poroelastic extension at the shallow basement rocks can increase $\Delta\tau$ during injection period, inducing earthquakes along the shallow fault zone. This may explain seismic activities observed at shallow depths of the basement [*Hornbach et al.*, 2016].

4.2 Effect of fault permeability

The fault permeability is important to determine the location and rate of earthquake occurrence. To emphasize the effect of the fault permeability, we increase the permeability of the Fault 2 ($k_{f2} = 1\times10^{-15}$ m^2, conductive but less permeable than Faults 1 and 3) to analyze how the permeability variation in multiple faults affects the change of pore pressure and stresses along each fault.

Compared to the reference case in Figure 3, pore pressure diffuses directly into the conductive Fault 2, which also decreases the positive change of $f\Delta p$ in the Fault 1 (Figure 6a). However, an intermediate permeability of Fault 2 retards the rate of diffusion, which accumulates pore pressure within the upper portion of Fault 2 (Figure 6b). The lateral propagation of the pressure across Fault 2 reaches Fault 3, which increases $f\Delta p$ along Fault 3 (Figure 6c). This case clearly demonstrates that seismic activities at shallow depths can be significantly influenced by fault zone architectures with varying hydrogeological and mechanical properties.

Pressurization-induced compression is developed along the fault zone where diffusion dominates, but extension occurs below the pressurized region (Figures 6d to 6f). Compared to the reference case of the sealing Fault 2 (Figure 3e), diffusion into the partially permeable Fault 2 compresses the shallow fault more significantly. This additional diffusion into the Fault 2 results in less diffusion into the Fault 1. Subsequently less dilation causes slight extension at deep fault zones.

Direct pore-pressure diffusion leads to positive changes in $\Delta\tau$ (Figures 6g to 6i) as well as R (Figures 6j to 6l). This shows that the fault permeability controls the extent of pressure front and poroelastic stressing within the fault zone, hence, the spatial distribution of $\Delta\tau$ and R vary along each fault. The major increases in $\Delta\tau$ and R are observed at the shallow Fault 2 ($R_{max} \approx 50$) because relatively less diffusivity slows down

the pressure propagation and accumulates pore pressure significantly. For more conductive faults (Fault 1 and 3), poroelastic compression attenuates $f\Delta p$ within/near the injection interval so that the increment in $\Delta\tau$ and R occurs at the deep fault zone. The lateral diffusion across Fault 2 decreases $\Delta\tau$ and R along Fault 1 ($R_{max} \approx 14$) while increases them along Fault 3 ($R_{max} \approx 5$) compared to the reference case.

Figure 7 shows the lateral distribution of $f\Delta p$, $\Delta\tau_s + f\Delta\sigma_n$, and $\Delta\tau$ in the horizontal plane of the reservoir ($z = 0.01$ km) at $t = 45$ days (post shut-in phase). The injection location is indicated by yellow star. Within the reservoir, diffusion of pore pressure is a dominant mechanism to determine $\Delta\tau$, and the fault instability is controlled mainly by the permeability of each fault. The sealing Fault 2 inhibits pore-pressure propagation across it, and the largest increases in $\Delta\tau$ is observed at the Fault 1 (Figures 7a to 7c). On the other hand, the conductive Fault 2 allows diffusion into/across it, and the substantial accumulation of pore pressure along the Fault 2 causes the largest increase in $\Delta\tau$ on it (Figures 7d to 7f). This comparative study suggests that the fault permeability controls the hydraulic and mechanical interaction between adjacent faults and/or surrounding formations, potentially determining the occurrence of injection-induced earthquakes.

4.3 Effect of model dimension

The 2-D aerial-view domain representing the lateral interface between the reservoir and basement (Figure 8) is used to evaluate the effect of model dimensionality (2-D vs. 3-D). All other conditions are the same as in the 3-D model. Assuming the plane strain condition in the (x,y)-plane, the fault dimension in the vertical direction is large enough to neglect the variability of applied forces as well as the boundary effect on fluid flow. The point data extracted at the center of the fault (i.e., star points in Figures 1 and 8) are used to compare the temporal evolution of pore pressure, stresses, stressing rate ($\dot{\tau}$) and the seismicity rate (R).

For the conductive faults (Faults 1 and 3), pore pressure in the 2-D domain increases faster and higher than in the 3-D model because pore pressure diffuses laterally only in the 2-D domain, but both lateral and vertical diffusion into upper and lower units is allowed in the 3-D domain (Figures 9a and 9c). Mechanically, the conductive faults are compressed due to poroelastic response to pressurization for both 3-D and 2-D models

(Figures 9d and 9f). For the 2-D sealing Fault 2, $f\Delta p$ increases positively, but the poroelastic stress is negative corresponding to poroelastic compression (Figures 9b and 9e). In the 3-D domain, the vertical displacement (i.e., dilation/shrinkage of basement rocks) is additionally engaged in poroelastic stressing, which results in transition from negative to positive $f\Delta p$ along Fault 2 after shut-in due to relaxation of poroelastic extension.

For both 2-D and 3-D models, the conductive Faults 1 and 3 are destabilized mainly by direct pore-pressure diffusion (Figures 9g and 9i). The confinement of pore pressure in the 2-D domain increases positive $\Delta\tau$ more significantly during injection (larger changes in $\dot{\tau}$, Figures 9j and 9l), subsequently increasing R by one order of magnitude (Figures 9m and 9o). On the other hand, the sealing Fault 2 can be either destabilized or stabilized depending on vertical poroelastic stressing associated with mechanical and hydraulic properties of surrounding units. In the 2-D domain, strong lateral compression develops by rapid pressure buildup around the Fault 2, which enhances the fault stability (negative $\Delta\tau$, Figure 9h) and prevents the earthquake occurrence (Figure 9n). Considering the vertical displacement in a 3-D multilayer system, poroelastic extension of the basement underneath the reservoir destabilizes the Fault 2 (refer to the Section 4.1), which cannot be described by the 2-D aerial view model.

Comparison of 2-D and 3-D modeling results clearly shows that restricting diffusion and deformation in the lateral direction in a 2-D aerial-view domain can over- or under-estimate the potential of seismic hazards along basement faults. In a 3-D domain, diffusion of pore pressure into the basement rock (not directly into the basement fault) reduces pore-pressure buildup within the conductive fault whereas it can induce poroelastic stressing on the sealing fault zone outside the pressurized region. Mechanical behaviors of each fault interacting with surrounding formations vary depending on the domain dimension and fault permeability. Note that 2-D vertical model could be useful to predict the potential of induced seismicity driven by fluid injection directly into the basement, as in enhanced geothermal systems. The dramatic variation in hydro-mechanical properties and fracture scales would be captured more precisely in a 2-D vertical domain at the current computational power. However, 2-D vertical model assumes the finite or semi-infinite geometry in the horizontal direction, which requires appropriate setting of boundary conditions and injection operation for proper estimates of magnitude and rate of possible seismic events. Only 3-D model can properly account for pore-pressure prop-

agation and rock deformation in the vertical and horizontal directions which are critical to determine the stability of basement faults. These results suggest that 3-D model with proper configuration and formation properties is essential to accurately estimate the seismic hazards associated with fluid injection.

5 Conclusions

We model multiple faults in a 3-D multilayer system to estimate the magnitude, rate and location of injection-induced earthquakes by considering poroelastic coupling effects. Neglecting poroelastic coupling effects causes less perturbations in pore pressure and thus underestimates $M_{\mathrm{W},max}$ at given injection scenarios. The $\bar{\mathbf{u}}$-based $M_{\mathrm{W},max}$ is less than the ΔV-based one because dissipation of pore pressure into upper mudrock and lower basement (not directly into the fault zone) causes less perturbations in stress/strain fields on individual faults.

Our 3-D modeling study emphasizes that the interaction between direct pore-pressure diffusion and poroelastic stressing can increase the rate of induced seismicity (R) along the fault of any hydraulic characteristics. However, the rate and location of earthquakes will vary depending on hydrogeological and mechanical properties of each fault (Table 3). Our key finds are summarized as follows:

- The highly conductive fault enhances pore-pressure diffusion into/across it where induced seismicity is predominantly caused by direct diffusion. The most frequent earthquakes occur along the conductive fault at deep depths because poroelastic compression within/near the injection interval stabilizes the upper fault zone. Along a fault further away from the injection well, poroelastic stressing driven by pressurization is less involved in the earthquake occurrence.
- The presence of sealing fault impedes pore-pressure propagation into/across the fault zone where perturbation in pore pressure is not expected. However, the mechanical behavior of the bounding formations compresses or extends the sealing fault corresponding to well operation. Note that the uncoupled system cannot describe the poroelastic behavior of the hydraulically isolated faults (e.g., sealing faults or basement faults at depth).
- The slightly conductive fault can attenuate the extent of pressurized region within the fault, but a high fraction of increased pore pressure is accumulated along the

fault (maximum $f\Delta p$ nearest to the injection interval), which can cause the significant increases in R at shallow depths in faults.

Although 2-D horizontal models can be computationally efficient, the potential seismic hazard can be over- or under-estimated by neglecting diffusion of pore pressure and deformation of the formation in the vertical direction. The confinement of pore-pressure diffusion in the 2-D reservoir tends to overestimate the rate of potential earthquakes along the conductive fault. The poroelastic stressing associated with upper and lower units in 3-D model induces the instability of the sealing fault, potentially inducing earthquakes even without direct diffusion, which cannot be accounted for by 2-D modeling approach.

Given the seismic hazards posed by fluid injection, therefore, the 3-D modeling of multiple fault systems including poroelastic coupling is required to develop proper responses and optimal injection practices to mitigate the uncertainty and risk of induced seismicity along the pre-existing faults associated with energy exploration or underground storage of fluids.

ACKNOWLEDGMENTS

The authors thank the reviewers and Editor Yehuda Ben-Zion for helpful comments. This work was supported by the Laboratory Directed Research and Development program at Sandia National Laboratories. Sandia National Laboratories is a multimission laboratory managed and operated by National Technology and Engineering Solutions of Sandia, LLC., a wholly owned subsidiary of Honeywell International, Inc., for the U.S. Department of Energys National Nuclear Security Administration under contract DE-NA-0003525. This paper describes objective technical results and analysis. Any subjective views or opinions that might be expressed in the paper do not necessarily represent the views of the U.S. Department of Energy or the United States Government. No data was used in producing this manuscript.

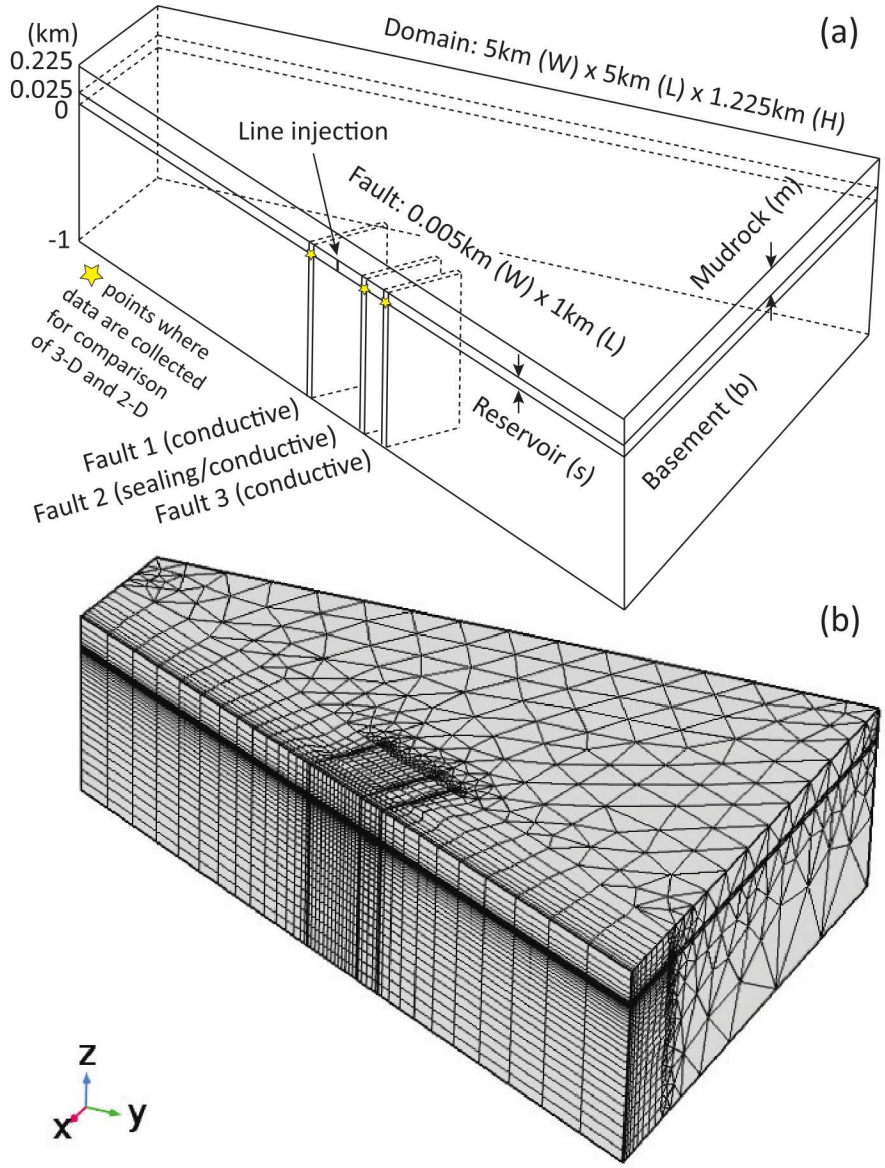

596 **Figure 1.** Schematic description of models in 3-D coordinate. Three vertical faults are mod-
597 eled in a three-layer system: two conductive faults (Fault 1 and 3) and a sealing fault (Fault 2)
598 for the reference model. Higher permeability is assigned on Fault 2 for the sensitivity test (refer
599 to Section 4.2). Fluids are injected between Fault 1 and Fault 2 at a constant rate of 0.02 kg/s/m
600 for 30 days.

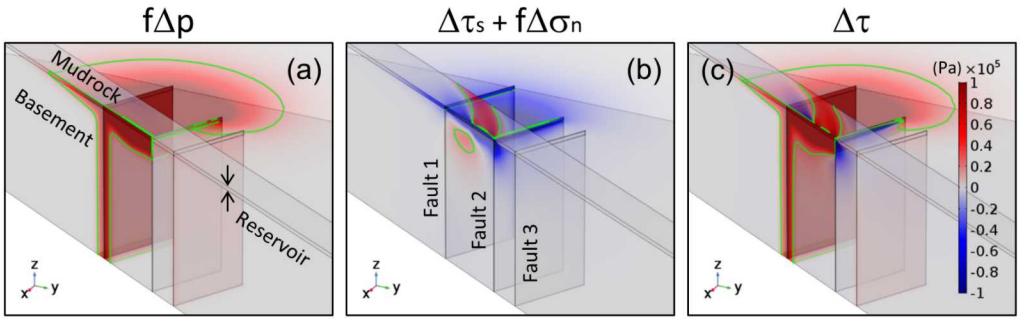

Figure 2. Spatial distributions of (a) pore pressure (Δp), (b) poroelastic stress ($\Delta\tau_s + f\Delta\sigma_n$), and (c) Coulomb stress ($\Delta\tau$) at the end of injection ($t = 30$ days). Positive and negative changes are shown in red and blue, respectively. A contour line of 2×10^4 Pa is shown in each plot to clarify the spatial distribution of pore pressure and stresses.

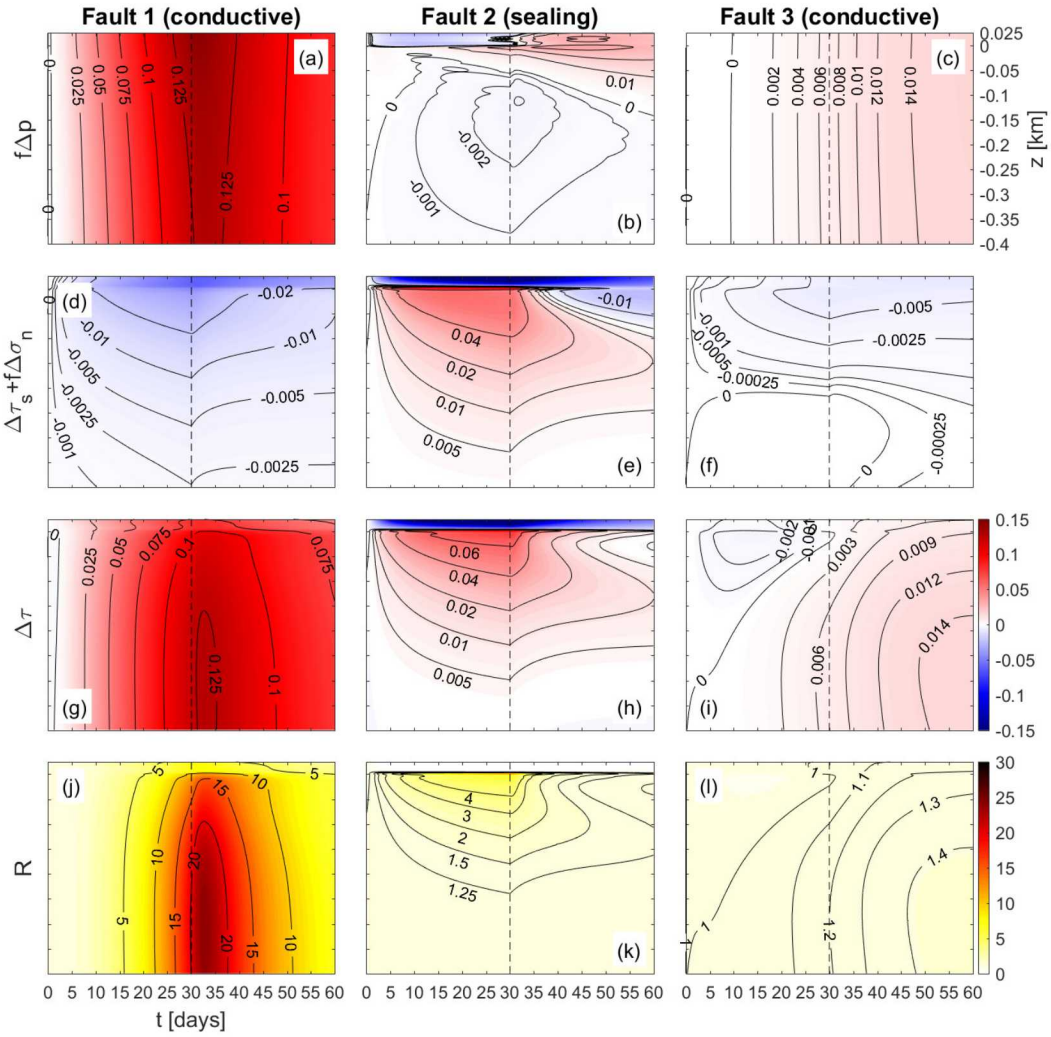

Figure 3. 3-D simulation results along each fault from top of the reservoir to the depth of -0.4 km in the coupled system. Temporal evolution of perturbations in (a–c) pore pressure (Δp), (d–f) poroelastic stress ($\Delta\tau_s + f\Delta\sigma_n$), (g–i) Coulomb stress ($\Delta\tau$), and (h–l) seismicity rate (R) is shown in the time-space domain (time in x-axis and depth in y-axis). Note that the same color scale is applied to $f\Delta p$, $\Delta\tau_s + f\Delta\sigma_n$ as shown in (a–i), and $\Delta\tau$. A vertical dash line at $t = 30$ days represents the end of injection.

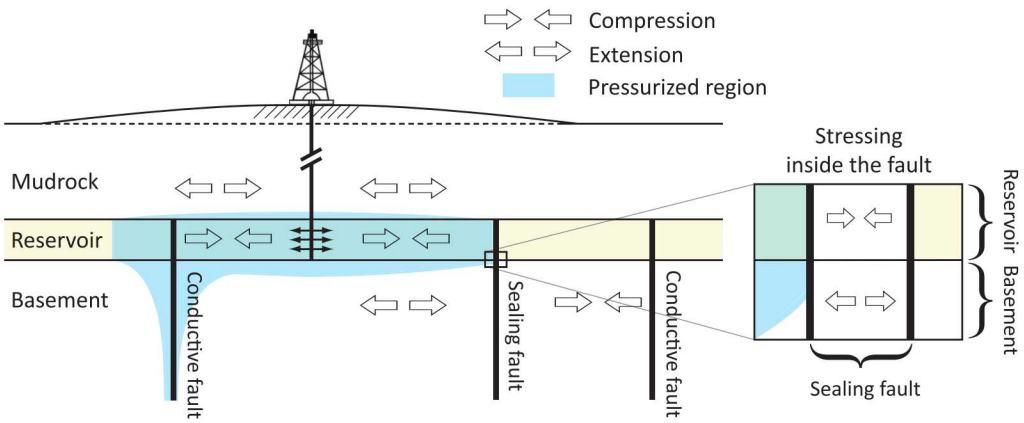

Figure 4. Schematics of poroelastic coupling mechanisms induced by fluid injection. Open arrows indicate lateral strains developed in the formation. The blue region represents the pressurized zone due to direct diffusion of pore pressure. Pore-pressure buildup generates compression within the pressurized zone as well as near the distant conductive fault, but causes extension nearby the pressurized zone due to the poroelastic response to fluid injection. Within the sealing fault, poroelastic stressing is determined by the pressurization of the bounding formation: compression at the upper portion bounded by strongly pressurized reservoir in a lateral direction while extension at the lower portion bounded by the basement rock.

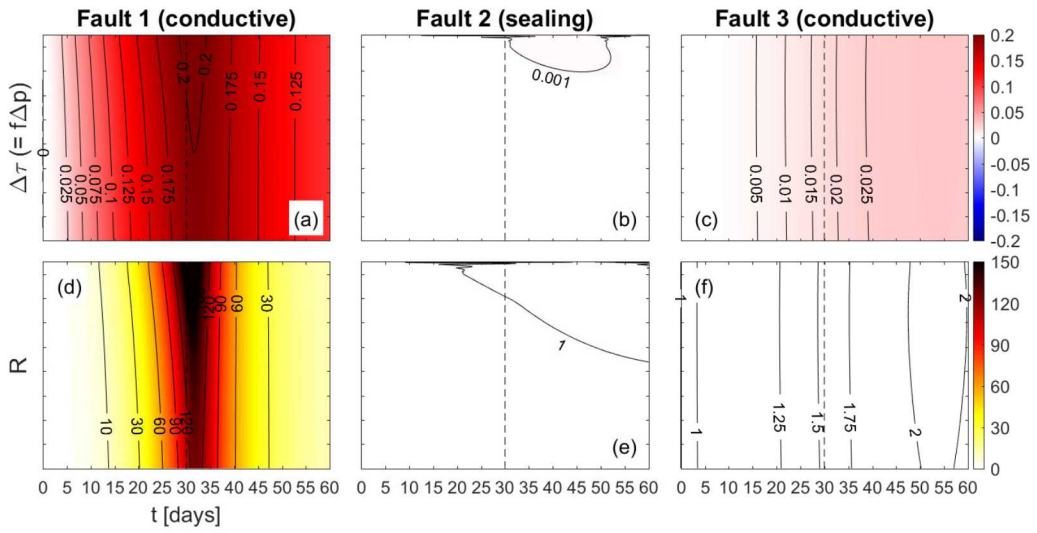

Figure 5. 3-D simulation results along each fault from top of the reservoir to the depth of -0.4 km in the uncoupled system. Temporal evolution of perturbations in (a–c) Coulomb stress ($\Delta\tau = f\Delta p$ in the uncoupled system) and (d–f) seismicity rate (R) is shown in the time-space domain (time in x-axis and depth in y-axis). A vertical dash line at $t = 30$ days represents the end of injection.

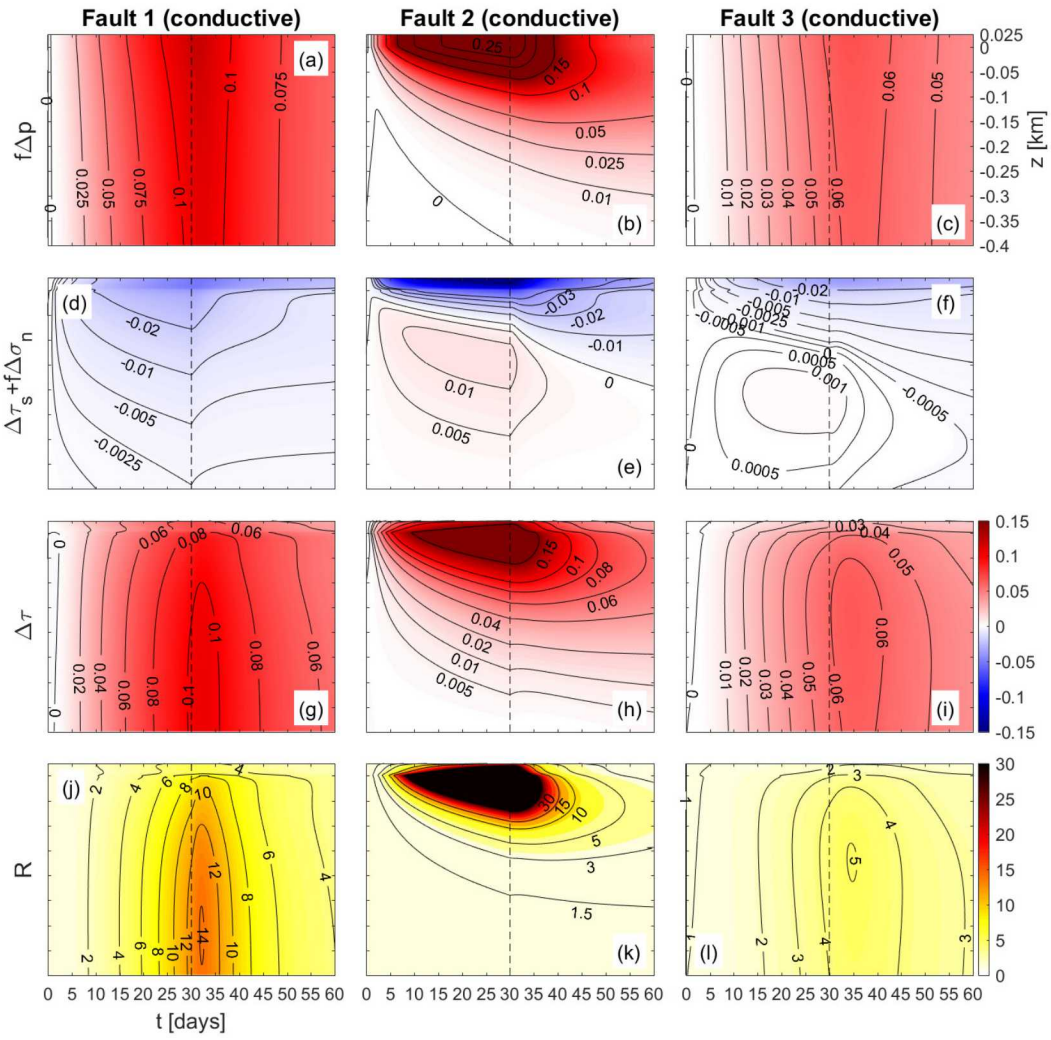

Figure 6. 3-D simulation results along each fault from top of the reservoir to the depth of -0.4 km. Larger permeability (1×10^{-15} m^2) is assigned to the Fault 2 to look into the fault permeability effect on injection-induced seismicity along each fault, which allows quantitative comparison to the result from the reference model where the Fault 2 is sealing (Figure 3). The plot format remains the same to Figure 3.

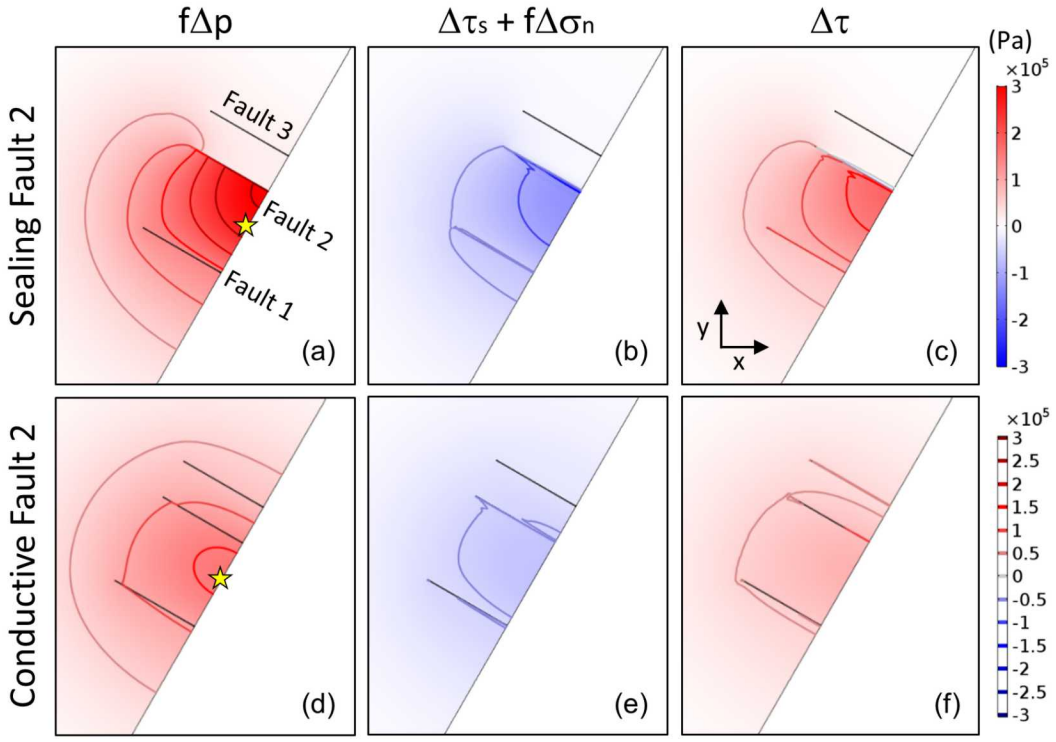

Figure 7. Comparison of 3-D simulation results at the interface between the reservoir and basement: top row for the sealing Fault 2 (reference case) and bottom row for the conductive Fault 2 (refer to Figures 3 and 6 for vertical distributions with time). The location of injection is indicated by a yellow star point.

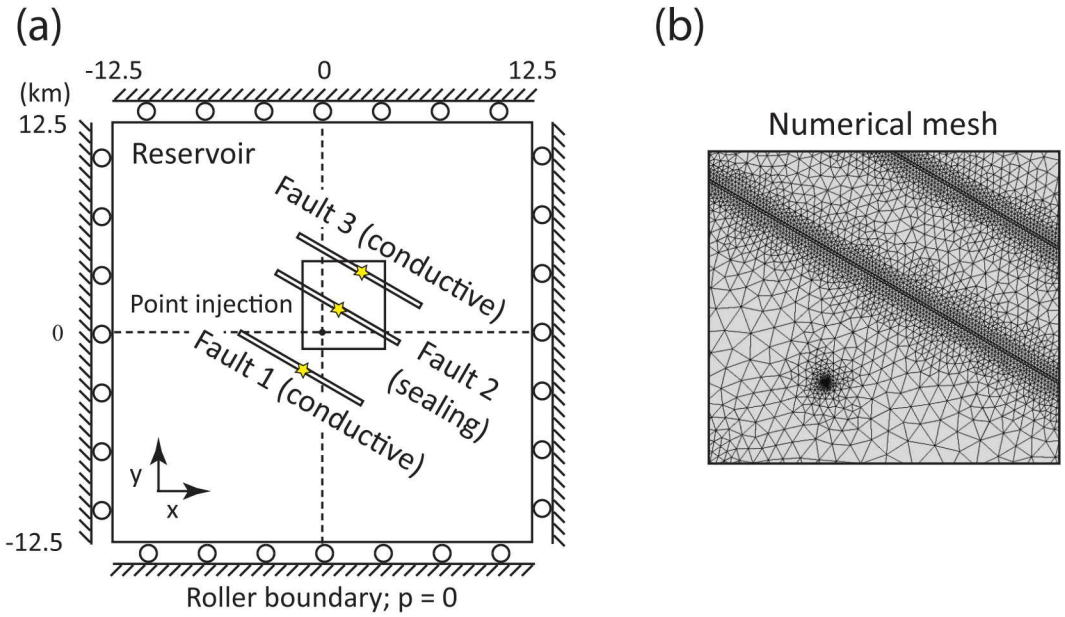

633 **Figure 8.** Schematic description of models in 2-D coordinate. The 2-D model represents the
634 horizontal interface between the reservoir and basement. Data are extracted from star points for
635 the comparative study of 2-D and 3-D models.

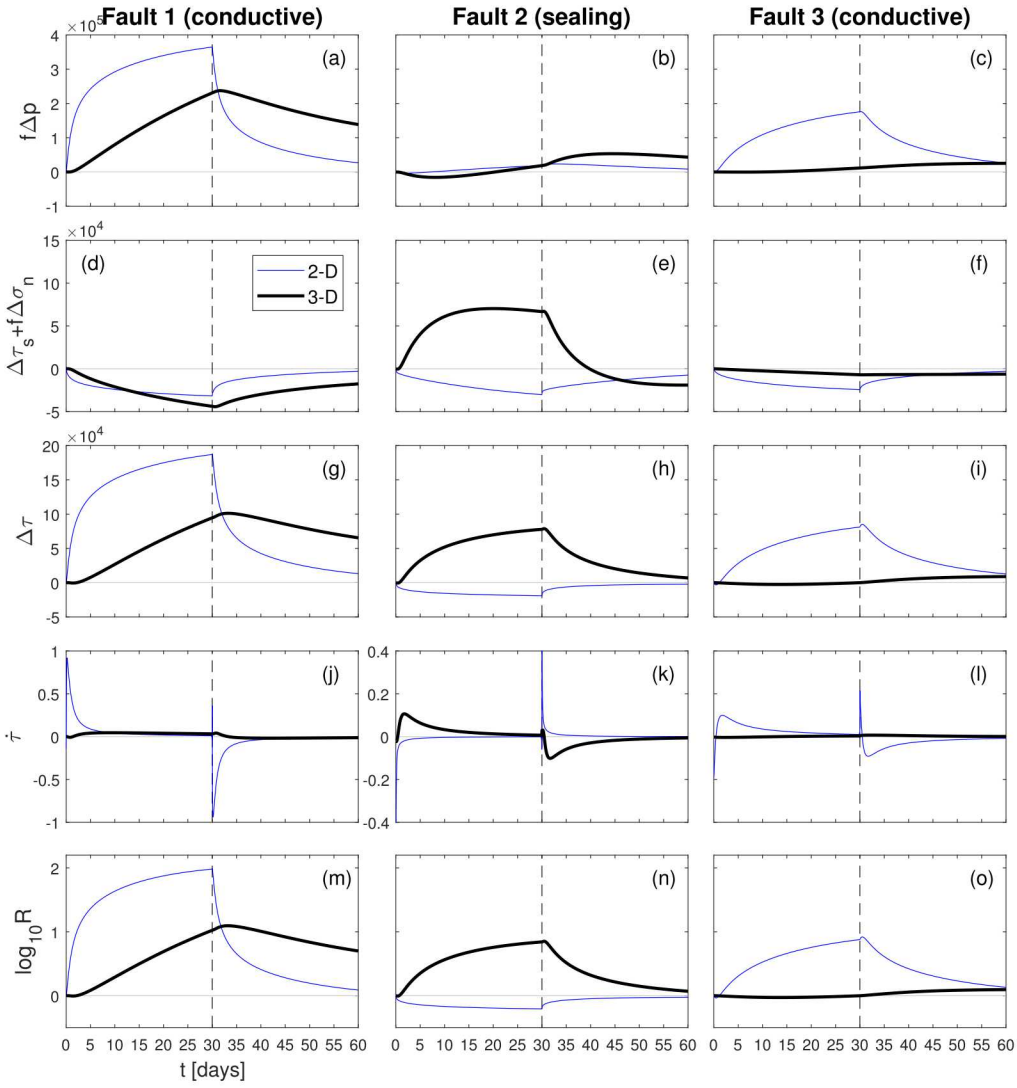

Figure 9. Comparison of 2-D and 3-D simulation results (point data over time). Temporal evolution of (a–c) pore pressure (Δp), (d–f) poroelastic stress ($\Delta\tau_s + f\Delta\sigma_n$), (g–i) Coulomb stress ($\Delta\tau$), (j–l), Coulomb stressing rate ($\dot{\tau}$) (m–o) logarithmic seismicity rate ($\log_{10}R$). Each row has the same scale of y-axis except (j–l) (the same scale is applied to (k–l), not (j)). A vertical dash line at $t = 30$ days represents the end of injection.

641 **Table 1.** Summary of Model Properties

Model properties	Mudrok	Reservoir	Basement	Fault	Fluid
k^* (m^2)	1×10^{-19}	1×10^{-14}	2×10^{-17}	$1\times10^{-12}/1\times10^{-21}$	-
ϕ (-)	0.1	0.25	0.05	0.02	-
G (GPa)	11.5	7.6	25	6	-
ν (-)	0.3	0.2	0.2	0.2	-
ν_u (-)	0.35	0.25	0.25	0.33	-
B (-)	0.8	0.62	0.85	0.62	-
f (-)	-	-	-	0.6	-
ρ (kg/m^3)	2600	2500	2740	2500	1000
$\eta^\dagger$ (Pa·s)	-	-	-	-	0.4×10^{-3}

$*$ End-member fault permeabilities for conductive and sealing fault. For the reference model, Fault 1 and 3 are conductive while Fault 2 is sealing for the reference model. Permeability of Fault 2 is enhanced ($k_{f2} = 1 \times 10^{-15}$ m^2) for the sensitivity test.

† Brine viscosity ranges $0.4\times10^{-3}(\pm0.05\times10^{-3})$ [*Hornbach et al.*, 2016].

642 **Table 2.** Estimate of the maximum earthquake magnitude

Governing parameter	Seismic moment relation	Seismic moment (M_0, N·m) / Maximum magnitude ($M_{\mathrm{W},max}$, -)* Overall formation	Fault 1	Fault 2	Fault 3
ΔV	Eqn. (6)†	1.08×10^{12} / 1.99	-	-	-
	Eqn. (7)‡	1.66×10^{12} / 2.11	-	-	-
$\bar{\mathbf{u}}$	Eqn. (9)	-	1.78×10^{11} / 1.47	1.20×10^{11} / 1.35	1.04×10^{11} / 1.31

∗ The upper bound to the earthquake magnitude ($M_{\mathrm{W},max}$) is computed by the moment-magnitude relation (10) with three different approaches of M_0 estimate.

† Refer to *McGarr* [2014].

‡ Including the poroelastic coupling effect.

643 **Table 3.** Summary of the poroelastic coupling effects depending on the fault permeability

Fault permeability	Coupled system, $\Delta\tau = (\Delta\tau_s + f\Delta\sigma_n) + f\Delta p$		
	$f\Delta p$	$\Delta\tau_s + f\Delta p$	R_{max}
Highly conductive	(+)	(–) along the whole zone	At the lower zone
Moderately conductive	(+) at the upper zone	(–) near the reservoir (+) outside the pressurized zone	At th upper zone
Sealing*	(–), but negligible	(–) within the reservoir (+) within the basement	At the uppermost bounded by the basement
	Uncoupled system, $\Delta\tau = f\Delta p$		
	$f\Delta p$	$\Delta\tau_s + f\Delta p$	R_{max}
Conductive	(+)	None	At the uppermost
Sealing*	(+), but negligible	None	Almost no seismicity

∗ If the sealing fault has lower permeability than one used in this study, almost no changes in $f\Delta p$ is expected.

A: Appendix A

The Biot formulation of the constitutive equations for a fluid-filled porous material is based on the assumptions of linearity between the stress and the strain, and the elastic reversibility of the deformation process. Assuming that pore space is fully saturated with fluid, the change in pore volume is equal to the variation of fluid volume trapped in the pore volume.

The first constitutive equation for the strain-stress relation can be expressed by selecting pore pressure (p) as the coupling term:

$$2G\epsilon_{ij} = \sigma_{ij} - \frac{\nu}{1+\nu}\sigma_{kk}\delta_{ij} + \frac{(1-2\nu)\alpha}{1+\nu}p\delta_{ij}, \tag{A.1}$$

where the subscripts i, j =1, 2, and 3 corresponding to the coordinate axes x, y, and z respectively. Using the volumetric strain (ϵ) as the coupling term yields the second constitutive equation for the pore fluid as follows:

$$p = \frac{BK_u}{\alpha}\left(\zeta - \alpha\epsilon\right) = \frac{1}{S}\left(\zeta - \alpha\epsilon\right), \tag{A.2}$$

where ζ (-) is the variation of fluid volume per unit volume of porous material, K_u (Pa) is the bulk modulus for undrained conditions ($\zeta = 0$), and the inverse of the constrained specific storage (S^{-1}, Pa) is the Biot's modulus to characterize the fluid increment in the porous medium as poroelastic response to fluid injection, given by

$$\frac{1}{S} = \left.\frac{\partial\zeta}{\partial p}\right|_{\epsilon=0}. \tag{A.3}$$

Constraining the control volume to be constant ($\epsilon = 0$) simplifies the pore pressure change in terms of the net injected fluid volume (ΔV):

$$\Delta p = \frac{1}{S}\frac{\Delta V}{V}. \tag{A.4}$$

The increase in pore pressure on average is assumed to be sufficient to induce earthquakes and the magnitude-frequency distribution can be described by the G-R relation. Following the same procedure done by *McGarr* [2014] the upper limit of seismic moment can be written as the equation (7).

References

Ake, J., K. Mahrer, D. O'Connell, and L. Block (2005), Deep-Injection and Closely Monitored Induced Seismicity at Paradox Valley, Colorado, *Bull. Seismol. Soc. Am.*, *95(2)*, 664–683, doi:10.1785/0120040072.

Arrowsmith, S. J., and L. Eisner (2006), A technique for identifying microseismic multiplets and application to the Valhall field, North Sea, *Geophys.*, *71(2)*, V31–V40, doi:10.1190/1.2187804.

Bachmann, C. E., S. Wiemer, B. P. Goertz-Allmann, and J. Woessner (2012), Influence of pore-pressure on the event-size distribution of induced earthquakes, *Geophys. Res. Lett.*, *39(9)*, L09,302, doi:10.1029/2012GL051480.

Bense, V. F., and M. A. Person (2006), Faults as conduit-barrier systems to fluid flow in siliciclastic sedimentary aquifers, *Water Resour. Res.*, *42(5)*, doi:10.1029/2005WR004480.

Biot, M. A. (1941), General theory of three-dimensional consolidation, *J. Appl. Phys.*, *12*, 155–164.

Caine, J. S., J. P. Evans, and C. B. Forster (1996), Fault zone architecture and permeability structure, *Geology*, *24*, 1025–1028, doi:10.1130/0091-7613(1996)024¡1025:FZAAPS¿2.3.CO;2.

Cappa, F., and J. Rutqvist (2011), Modeling of coupled deformation and permeability evolution during fault reactivation induced by deep underground injection of CO_2, *Int. J. Greeh. Gas Con.*, *5(2)*, 336–346, doi:10.1016/j.ijggc.2010.08.005.

Chang, K. W., and P. Segall (2016a), Injection induced seismicity on basement faults including poroelastic stressing, *J. Geophys. Res. Solid Earth*, *121(4)*, 2708–2726, doi:10.1002/2015JB012561.

Chang, K. W., and P. Segall (2016b), Seismicity on basement faults induced by simultaneous fluid injection-extraction, *Pure Appl. Geophys.*, *173(8)*, 2621–2636, doi:10.1007/s00024-016-1319-7.

Chang, K. W., H. Yoon, and M. J. Martinez (2018), Seismicity rate surges after shut-in: poroelastic response to fluid injection, *Bull. Seismol. Soc. Am.*, p. in press, doi:10.1785/0120180054.

COMSOL Multiphysics (2017), COMSOL Multiphysics User's Guide, COMSOL AB, Burlington, Mass.

Day, R., and D. Potts (1994), Zero thickness interface elementsnumerical stability and application, *Int. J. Numer. Anal. Methods Geomech.*, *18(10)*, 689–708, doi:10.1002/nag.1610181003.

De Simone, S., J. Carrera, and V. Vilarrasa (2017), Superposition approach to understand triggering mechanisms of post-injection induced seismicity, *Geothermics*, *70*, 85–97, doi:10.1016/j.geothermics.2017.05.011.

Dempsey, D., J. Suckale, and Y. Huang (2016), Collective properties of injection-induced earthquake sequences: 2. spatiotemporal evolution and magnitude frequency distributions, *J. Geophys. Res. Solid Earth*, *121(5)*, 3638–3665, doi:10.1002/2015JB012551.

Detournay, E., and A. H. Cheng (1993), Fundamentals of poroelasticity, in Comprehensive Rock Engineering: Principles, Practics & Projects, vol. 2, Analysis and Design Method, edited by C. Fairhurst, chap. 5, pp. 113–170, Pergamon, Tarrytown, N.Y.

Dieterich, J. H. (1994), A constitutive law for rate of earthquake production and its application to earthquake clustering, *J. Geophys. Res. Solid Earth*, *99(B2)*, 2601–2618, doi:10.1029/93JB02581.

Doser, D. I., M. R. Baker, M. Luo, P. Marroquin, L. Ballesteros, J. Kingwell, H. L. Diaz, and G. Kaip (1992), The not so simple relationship between seismicity and oil production in the Permian Basin, west Texas, *Pure Appl. Geophys.*, *139(3-4)*, 481–506, doi:10.1007/BF00879948.

Dreij, K., Q. A. Chaudhry, B. Jernstrom, R. Morgenstern, and M. Hanke (2011), A method for efficient calculation of diffusion and reactions of lipophilic compounds in complex cell geometry, *PLoS One*, *6(8)*, 1–18.

Duan, B., and D. D. Oglesby (2006), Heterogeneous fault stresses from previous earthquakes and the effect on dynamics of parallel strike-slip faults,, *J. Geophys. Res. Solid Earth*, *111*, B05,309, doi:doi:10.1029/2005JB004138.

Ellsworth, W. L. (2013), Injection-induced earthquakes, *Science*, *341*(6142), doi:10.1126/science.1225942.

Figueiredo, B., C.-F. Tsang, J. Rutqvist, J. Bensabat, and A. Niemi (2015), Coupled hydro-mechanical processes and fault reactivation induced by CO_2 injection in a three-layer storage formation, *Int. J. Greenh. Gas Con.*, *39*, 432–448, doi:10.1016/j.ijggc.2015.06.008.

Gambolati, G., P. Teatini, D. Bau, and M. Ferronato (2010), Importance of poroelastic coupling in dynamically active aquifers of the Po river basin, Italy, *Water Resour. Res.*, *36*(9), 2443–2459, doi:10.1029/2000WR900127.

Giardini, D. (2009), Geothermal quake risks must be faced, *Nature*, *462*, 848–849, doi:10.1038/462848a.

Gudmundsson, A., T. H. Simmenes, B. Larsen, and S. L. Philipp (2010), Effects of internal structure and local stresses on fracture propagation, deflection, and arrest in fault zones, *J. Struct. Geol.*, *32*(11), 1643–1655, doi:10.1016/j.jsg.2009.08.013.

Hanks, T. C., and H. Kanamori (1979), A moment magnitude scale, *J. Geophys. Res.*, *84(5)*, 2348–2350, doi:10.1029/JB084iB05p02348.

Hearn, E. H., C. Koltermann, and J. L. Rubinstein (2018), Numerical Models of Pore Pressure and Stress Changes Along Basement Faults Due to Wastewater Injection: Applications to the 2014 Milan, Kansas Earthquake, *Geochem. Geophy. Geosy.*, *19*, 11,778–1198, doi:10.1002/2017GC007194.

Hills, R. (2000), Pore pressure/stress coupling and its implications for seismicity, *Explor. Geophys.*, *31(1–2)*, 448–454.

Hornbach, M. J., H. R. DeShon, W. L. Ellsworth, B. W. Stump, C. Hayward, C. Frohlich, H. R. Oldham, J. E. Olson, M. B. Magnani, C. Brokaw, and J. H. Luetgert (2015), Casual factors for seismicity near azle, texas, *Nature Communications*, *6*, 6728, doi:10.1038/ncomms7728.

Hornbach, M. J., M. Jones, M. Scales, H. R. DeShon, M. B. Magnani, C. Frohlich, B. Stump, C. Hayward, and M. Layton (2016), Ellenburger wastewater injection and seismicity in north texas, *Phys. Earth Planet. In.*, *261*, 54–68, doi:10.1016/j.pepi.2016.06.012.

Horton, S. (2012), Disposal of hydrofracking waste water fluid by injection into subsurface aquifers triggers earthquake swarm in Central Arkansas with potential for damaging earthquake, *Seismol. Res. Lett.*, *83(2)*, 250–260, doi:10.1785/gssrl.83.2.250.

Hough, S. E. (2014), Shaking from injection-induced earthquakes in the central and eastern United States, *Bull. Seismol. Soc. Am.*, *104(5)*, 2619, doi:10.1785/0120140099.

Hubbert, M. K., and W. W. Rubbey (1959), Role of fluid pressure in mechanics of overthrust faulting, *Geol. Soc. Am. Bull.*, *70(2)*, 115–166, doi:10.1130/0016-

7606(1959)70[115:ROFPIM]2.0.CO;2.

Hughes, T. J. R. (2000), *The Finite Element Method: Linear Static and Dynamic Finite Element Analysis*, Courier Dover Publ., Mineola, NY.

Jha, B., and R. Juanes (2007), A locally conservative finite element framework for the simulation of coupled flow and reservoir geomechanics, *Acta Geotechnica*, *2(3)*, 139–153, doi:10.1007/s11440-007-0033-0.

Jha, B., and R. Juanes (2014), Coupled multiphase flow and poromechanics: A computational model of pore pressure effects on fault slip and earthquake triggering, *Water Resour. Res.*, *50(5)*, 3776–38,083, doi:10.1002/2013WR015175.

Kanamori, H., and E. E. Brodsky (2001), The physics of earthquakes, *Physics Today*, *54(6)*, 34–40, doi:10.1063/1.1387590.

Kerenan, K. M., H. M. Savage, G. A. Abers, and E. S. Cochran (2013), Potentially induced earthquakes in Oklahoma, USA: Links between wastewater injection and the 2011 M_w 5.7 earthquake sequence, *Geology*, *41*, 699–702, doi:10.1130/G34045.1.

Kerenan, K. M., M. Weingarten, G. A. Abers, B. A. Bekins, and S. Ge (2014), Sharp increase in central Oklahoma seismicity since 2008 induced by massive wastewater injection, *Science*, *345*, 448, doi:10.1126/science.1255802.

Kim, J., H. A. Tchelepi, and R. Juanes (2011), Stability and convergence of sequential methods for coupled flow and geomechanics: Fixedstress and fixed-strain splits, *Comput. Methods Appl. Mech. Eng.*, *200(13)*, 1591–1606, doi:10.1016/j.cma.2010.12.022.

Kim, W. Y. (2013), Induced seismicity associated with fluid injection into a deep well in Youngstown, Ohio, *J. Geophys. Res.*, *118(7)*, 3506–3518, doi:10.1002/jgrb.50247.

Langenbruch, C., and M. D. Zoback (2016), How will induced seismicity in Oklahoma respond to decreased saltwater injection rates?, *Science Advances*, *2(11)*, e1601,542, doi:10.1126/sciadv.1601542.

Maerten, L., P. Gillespie, and D. D. Pollard (2002), Effects of local stress perturbation on secondary fault development, *J. Struct. Geol.*, *24(1)*, 145–153, doi:doi.org/10.1016/S0191-8141(01)00054-2.

McGarr, A. (2014), Maximum magnitude earthquakes induced by fluid injection, *J. Geophys. Res.*, *119(2)*, 1008–1019, doi:10.1002/2013JB010597.

Mogi, K. (1962), Magnitude-frequency relationship for elastic shocks accompanying fractures of various materials and some related problems in earthquakes, *Bull. Earthquake Res. Inst. Univ. Tokyo*, *40*, 831–853.

Nakai, J. S., M. Weingarten, A. F. Sheehan, S. L. Bilek, and S. Ge (2017), A Possible Causative Mechanism of Raton Basin, New Mexico and Colorado Earthquakes Using Recent Seismicity Patterns and Pore Pressure Modeling, *J. Geophys. Res. Solid Earth*, *122(10)*, 8051–8065, doi:10.1002/2017JB014415.

Pan, F., K. Sepehrnoori, and L. Y. Chin (2009), A New Solution Procedure for a Fully Coupled Geomechanics and Compositional Reservoir Simulator, *SPE Reservoir Simulation Symposium*, pp. SPE–119,029–MS, doi:10.2118/119029-MS.

Parson, T. (2002), Post1906 stress recovery of the San Andreas fault system calculated from threedimensional finite element analysis, *J. Geophys. Res. Solid Earth*, *107(B8)*, ESE 3–1–ESE 3–13, doi:10.1029/2001JB001051.

Rice, J. R., and M. P. Cleary (1976), Some basic stress diffusion solutions for fluid-saturated porous media with compressible constituents, *Rev. Geophys.*, *14*, 227–241, doi:10.1029/RG014i002p00227.

Rinaldi, A. P., P. Jeanne, J. Rutqvist, F. Cappa, and Y. Guglielmi (2014), Effects of faultzone architecture on earthquake magnitude and gas leakage related to CO_2 injection in a multilayered sedimentary system, *Greenh. Gases Sci. Technol.*, *4(1)*, 99–120, doi:10.1002/ghg.1403.

Rinaldi, A. P., V. Vilarrsa, J. Rutqvist, and F. Cappa (2015), Fault reactivation during CO_2 sequestration: Effects of well orientation on seismicity and leakage. , *Greenh. Gases Sci. Technol.*, *5(5)*, 645–656, doi:10.1002/ghg.1511.

Rubinstein, J. L., W. L. Ellsworth, A. McGarr, and H. M. Benz (2014), The 2011-present induced earthquake sequence in the raton basin of northern new mexico and southern colorado, *Bull. Seismol. Soc. Am.*, *104*(5), 2162–2181, doi:10.1785/0120140009.

Rutqvist, J., A. P. Rinaldi, F. Cappa, and G. J. Morris (2015), Modeling of fault activation and seismicity by injection directly into a fault zone associated with hydraulic fracturing of shale-gas reservoirs, *J. Pet. Sci. Eng.*, *127*, 377–386, doi:10.1016/j.petrol.2015.01.019.

Rutqvist, J., A. P. Rinaldi, F. Cappa, P. Jeanne, A. Mazzoldi, L. Urpi, Y. Guglielmi, and V. Vilarrasa (2016), Fault activation and induced seismicity in geological

carbon storage – lessons learned from recent modeling studies, *J. Rock Mech. Geotech. Eng.*, *8*(6), 789–804, doi:10.1016/j.jrmge.2016.09.001.

Seeber, L., J. G. Armbruster, and W. Y. Kim (2004), A fluid-injection-triggered earthquake sequence in Ashtabula, Ohio: implications for seismogenesis in stable continental regions, *Bull. Seismol. Soc. Am.*, *94*(1), 76–87, doi: 10.1785/0120020091.

Segall, P. (1989), Earthquakes triggered by fluid extraction?, *Geology*, *17*(10), 942–946, doi:10.1130/0091-7613(1989)017¡0942:ETBFE¿2.3.CO;2.

Segall, P. (2010), *Earthquake and Volcano Deformation*, Princeton University Press, Princeton, NJ.

Settari, A., and F. Mourits (1998), A coupled reservoir and geomechanical simulation system, *SPE J.*, *3*(3), 219–226, doi:10.2118/50939-PA.

Settari, A., and D. A. Walters (2001), Advances in coupled geomechanical and reservoir modeling with applications to reservoir compaction, *SPE J.*, *6*(3), 334–342, doi:10.2118/74142-PA.

Shapiro, S. A., O. Kruger, C. Dinske, and C. Langenbruch (2011), Magnitudes of induced earthquakes and geometric scales of fluid-stimulated rock volumes, *Geophysics*, *76(6)*, WC55–WC63, doi:10.1190/GEO2010-0349.1.

Stein, R. S. (1999), The role of stress transfer in earthquake occurrence, *Nature*, *402*, 605–609, doi:10.1038/45144.

Tran, D., A. Settari, and L. Nghiem (2004), New Iterative coupling between a reservoir simulator and a geomechanics module, *Energy Procedia*, *9(3)*, 362–369, doi: 10.2118/88989-PA.

Verdon, J. P. (2014), Significance for secure CO_2 storage of earthquakes induced by fluid injection, *Environ. Res. Lett.*, *9(6)*, 064,022, doi:10.1088/1748-9326/9/6/064022.

Vilarrasa, V., R. Makhnenko, and S. Gheibi (2016), Geomechanical analysis of the influence of CO_2 injection location on fault stability, *J. Rock Mech. Geotech. Eng.*, *8(6)*, 805–818, doi:10.1016/j.jrmge.2016.06.006.

Wang, H. F. (2000), *Theory of Linear Poroelasticity*, Princeton University Press, Princeton, NJ.

Warren, N. W., and G. V. Latham (1970), An experiment study of thermal induced microfracturing and its relation to volcanic seismicity, *J. Geophys. Res.*, *75*(23),

4455–4464, doi:10.1029/JB075i023p04455.

Weingarten, M., S. Ge, J. W. Godt, B. A. Bekins, and J. L. Rubinstein (2015), High-rate injection is associated with the increase in U.S. mid-continent seismicity, *Science*, *348(6241)*, 1336–1340, doi:10.1126/science.aab1345.

Wheeler, M. F., and X. Gai (2007), Iteratively coupled mixed and galerkin finite element methods for poroelasticity, *Numer. Methods Partial Differential Equations*, *23*(4), 785–797, doi:10.1002/num.20258.

White, J. A., and R. I. Borja (2011), Blockpartitioned NewtonKrylov solvers for fully coupled flow and geomechanics, *Comput. Geosci.*, *15*, 647–659, doi:10.1007/s10596-011-9233-7.

White, J. A., and W. Foxall (2016), Assessing induced seismicity risk at CO_2 storage projects: Recent progress and remaining challenges, *Int. J. Greenh. Gas Con.*, *49*, 413–424, doi:10.1016/j.ijggc.2016.03.021.

Wibberley, C. A., G. Yielding, and G. D. Toro (2008), Recent advances in the understanding of fault zone internal structure: a review, *Geological Society, London, Special Publications*, *299(1)*, 5–33, doi:10.1144/SP299.2.

Wyss, M. (1973), Towards a physical understanding of the earthquake frequency distribution, *Geophys. J. Int.*, *31*(4), 341–359, doi:10.1111/j.1365-246X.1973.tb06506.x.

Zbinden, D., A. P. Rinaldi, L. Urpi, and S. Wiemer (2017), On the physics-based processes behind production-induced seismicity in natural gas fields, *J. Geophys. Res. Solid Earth*, *122*(5), 3792–3812, doi:10.1002/2017JB014003.

Zhang, Y., M. Person, J. Rupp, K. Elett, M. A. Celia, C. W. Gable, B. Bowen, J. Evans, L. Bandilla, P. Mozley, T. Dewers, and T. Elliot (2013), Hydrogeologic controls on induced seismicity in crystalline basement rocks due to fluid injection into basal reservoirs, *Ground Water*, *51(4)*, 525–538, doi:10.1111/gwat.12071.

Zimmermann, R. W. (2000), Coupling in poroelasticity and thermoelasticity, *Int. J. Rock Mech. Min. Sci.*, *37*(1–2), 79–87.

Zoback, M. D., and J. H. Healy (1992), In situ stress measurements to 3.5 km depth in the Cajon Pass Scientific Research Borehole: Implications for the mechanics of crustal faulting, *J. Geophys. Res.*, *97*(B4), 5039–5057, doi:10.1029/91JB02175.